NMR Solution Structure of the 32-kDa Platelet Factor 4 ELR-Motif N-Terminal Chimera: A Symmetric Tetramer[†,‡]

Kevin H. Mayo,* Vikram Roongta, Elena Ilyina, Robert Milius, and Sharon Barker

Department of Biochemistry, Biomedical Engineering Center, University of Minnesota, 420 Delaware Street, S.E., Minneapolis, Minnesota 55455

Christopher Quinlan, Greg La Rosa, and Thomas J. Daly

Repligen Corporation, One Kendall Square, Building 700, Cambridge, Massachusetts 02139

Received May 17, 1995; Revised Manuscript Received July 12, 1995[⊗]

ABSTRACT: Native human platelet factor 4 (PF4) is a homotetrameric protein (70 residues/subunit) known for its anticoagulant heparin binding activity. 2D $^{15}N-^{1}H$ HSQC NMR experiments of native PF4 in solution show the presence of conformational heterogeneity consistent with the formation of asymmetric homo-tetramers as observed in the X-ray crystal structure of both human and bovine PF4. A chimeric mutant of PF4 (called PF4-M2) which substitutes the first 11 N-terminal residues for the first eight residues from homologous interleukin-8 forms symmetric homotetramers with essentially the same heparin binding activity as native PF4. The solution structure of PF4-M2 has been investigated by using two- and three-dimensional ^{1}H- and ^{15}N-NMR spectroscopy and NOE-restrained simulated annealing molecular dynamics. As with other members of the CXC chemokine family whose structures are known, the PF4-M2 subunit monomer consists of a mostly hydrophobic, triple-stranded antiparallel β-sheet onto which is folded an amphipathic C-terminal helix and a less periodic N-terminal domain. Although N-terminal substitution with the less acidic interleukin-8 sequence most affects the quarternary structure relative to native PF4 at the AC and AD dimer interfaces, AB dimer stability is weakened as reflected in reduced equilibrium association binding constants.

Human platelet factor 4 (PF4)[1] is a low molecular weight (70 amino acid residues; Deuel et al., 1977), heat-stable protein which is secreted by platelets (Holt & Niewiarowski, 1985) in a complex with a high molecular weight proteoglycan carrier (Huang et al., 1982). Under physiological conditions, PF4 exists as a tetramer (Mayo & Chen, 1989) and neutralizes the anticoagulant activity of heparin (Rucinski et al., 1979), a polysulfated glycosaminoglycan which acts to promote antithrombin-III inhibition of factor Xa and thrombin in the blood clotting cascade (Davie et al., 1991). PF4 also binds with unusually high affinity to insolubilized heparin and binds to other less sulfated glycosaminoglycans with lower affinity (Barber et al., 1972). In the presence of an excess of heparin (MW 10 000 cutoff), the typical PF4−heparin complex consists of one 32−34 saccharide long heparin molecule per protein tetramer (Loscalzo et al., 1985), although two hexadecasaccharides also can bind to one PF4 molecule (Bock et al., 1980).

PF4, which belongs to a family of CXC chemokines (Wolpe & Cerami, 1989), demonstrates other physiological effects, some of which may be related to binding heparin-like glycosaminoglycans on the surface of cells. PF4 is chemotactic for white blood cells (Deuel et al., 1981), inhibits megakaryocytopoiesis (Gerwitz et al., 1989; Han et al., 1990), angiogenesis (Maione et al., 1990), solid tumor growth (Sharpe et al., 1990), and vascular endothelial cell migration (Sato et al., 1990).

X-ray crystallographic studies of bovine (St. Charles et al., 1989) and human (Zhang et al., 1993) tetrameric PF4 show that, in both, subunit monomers have a three-stranded antiparallel β-sheet "scaffold" onto which is folded an aperiodic N-terminal domain and an amphipathic C-terminal α-helix which contains two pairs of lysine residues proposed to be important for binding heparin (Deuel et al., 1977; Loscalzo et al., 1985). In both human and bovine crystal structures, the homotetrameric arrangement of A, B, C, and D subunits is asymmetric. For human PF4 (Zhang et al., 1994), superposition of the four monomer subunits gives rms deviations (residues 8−70) of 1.05 Å for all backbone positions and 1.73 Å for all non-hydrogen atoms. AB type dimer rmsd values are similar, indicating that all monomer subunits and AB dimers are relatively well defined and superimposable. AC- and AD-type dimers, which give average rmsd values of 4.3 and 4.8 Å, respectively, therefore

[†] This work was supported by research support from the National Heart, Lung, and Blood Institute and Repligen Corporation to K.H.M. and by an American Heart Association, Minnesota Affiliate, Postdoctoral Fellowship to E.I.

[‡] Structural coordinates have been deposited with the Brookhaven Protein Data Bank under the code 1PFM.

* Send correspondence to this author.

[⊗] Abstract published in *Advance ACS Abstracts,* September 1, 1995.

[1] Abbreviations: PF4, platelet factor 4; LA-PF4, low-affinity-PF4; PF4-M2, platelet factor 4 chimeric mutant replacing the first ten PF4 residues with the first eight N-terminal residues from interleukin-8; PBP, platelet basic protein; βTG, β-thromboglobulin; NAP-2, neutrophil activating peptide-2; CTAP-III, connective tissue activating protein-III; IL-8, interleukin-8; NMR, nuclear magnetic resonance spectroscopy; 2D-NMR, two-dimensional NMR spectroscopy; NOE, nuclear Overhauser effect; NOESY, 2D-NMR nuclear Overhauser effect spectroscopy; rf, radio frequency; FID, free induction decay; CD, circular dichroism; HPLC, high-performance liquid chromatography; DG, distance geometry; M, monomer; D, dimer; T, tetramer; DSS, disuccinimidyl suberate; 3D-NMR, three-dimensional NMR; HOHAHA, homonuclear Hartmann−Hahn 2D-NMR spectroscopy; HSQC, heteronuclear single quantum coherence.

0006-2960/95/0434-11399$09.00/0

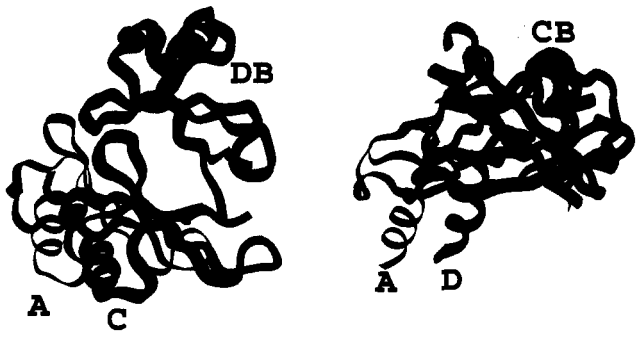

FIGURE 1: Superposition of one subunit each from AD- (left) and AC-type dimers (right) from the X-ray structure of native PF4 (Zhang et al., 1994).

account for the tetrameric asymmetry. Much of the asymmetry within the native PF4 tetramer can be accounted for by a 10° pseudo-C2-axis rotation of one AC dimer relative to the other (BD dimer) as illustrated in Figure 1. Due to this translocation, AD-type dimer interactions are weakest. Regions which are most affected by this asymmetry are the N-terminal residues and the turn/loop residues R22−S26, G33−T38, and T44−R49. Similar conclusions can be reached from analysis of the crystal structure of bovine PF4 (St. Charles et al., 1989).

In the crystal state, PF4 tetrameric asymmetry may be, at least in part, the result of heavy metal isomorphous replacement (St. Charles et al., 1989) or crystal lattice forces (Zhang et al., 1994). On the other hand, PF4 tetrameric asymmetry may be natural and play a role in heparin binding. The present study shows that the NMR solution conformation of native human PF4 is also asymmetric. Moreover, investigation of a human PF4 chimeric mutant which replaces the first 11 residues from the PF4 N-terminal sequence with the first eight residues from homologous interleukin-8 (IL-8) containing the IL-8 ELR tripeptide neutrophil activating motif (Clark-Lewis et al., 1993) shows that this mutant (called PF4-M2) forms symmetric homotetramers, indicating the importance of the highly negatively charged native PF4 N-terminal segment in dictating tetramer asymmetry. PF4-M2 provides a good "NMR friendly" protein whose solution structure is presented here and lays the groundwork for PF4−heparin binding studies currently underway in this lab.

MATERIALS AND METHODS

Isolation of Recombinant PF4. The synthetic genes for human native PF4 and PF4-M2 chimeric mutant were expressed as a nonfusion protein in *Escherichia coli* (BL21) cells and grown at the 10-L scale with ^{15}N-enriched ammonia as the nitrogen source. PF4 species were purified, cleaved, and refolded essentially as previously described (Yang et al., 1994). Purity was asessed by Coomassie staining of SDS−PAGE, analytical C4 reverse-phase HPLC, and amino acid analysis. Typically, several hundred milligrams of greater than 95% pure material was isolated from 100 g of starting material. Here, the term "native PF4" is used to refer to recombinant PF4 with the native PF4 sequence.

Determination of Protein Concentration. Protein concentrations were determined using the bicinchoninic acid (BCA) assay (Smith et al., 1985) and calculated on the basis of protein concentrations obtained from a standard dilution series of bovine serum albumin. Amino acid analysis of these chemokines was obtained following hydrolysis of the proteins for 24 h at 90 °C in 12 M HCl. Samples then were derivatized and analyzed according to the method of Bidlingmeyer et al. (1984). Protein concentrations also were checked by the methods of Lowry et al. (1951) and Waddell (1956).

Solution-Based Fluorescein-Derivatized Heparin Binding Assay. Binding of PF4-related proteins was examined through monitoring of quenching of heparin-based fluorescence. Fluorescein-derivatized heparin (F-hep) (Suda et al., 1990) was added to 3 mL of phosphate-buffered saline (PBS). Excitation and emission were monitored at 488 and 520 nm, respectively. Protein was titrated in small volume aliquots, with changes in fluorescence intensity being observed between each protein addition. Titration curves were corrected for dilution and photobleaching effects by titration of F-hep with buffer controls. Following each protein addition, 5-min incubations were performed to reach the new equilibrium. Data were plotted as the concentration of protein versus fraction of the maximal quenching of the corrected curves. Equilibrium binding constants were determined at the concentration of protein at 50% fluorescence quenching.

Factor X Heparin Binding Assay. Factor X assays were performed using a 96-well microtiter plate format. Buffer containing 10 mM Tris-HCl, pH 8.0, and 150 mM NaCl was incubated with 15 μL of heparin (3 units/mL; Upjohn), 15 μL of antithrombin III (6 units/μL; Boehringer Mannheim), and 15 μL Chromozym X (6 mM stock concentration; Boehringer Mannheim). The appropriate concentration of PF4 or PF4-M2 was added to the reaction mixture and incubated at RT for 30 min. At time 0, 15 μL of 0.1 unit/mL of factor Xa (Boehringer Mannheim) was added to start the reaction. The final volume of the reaction was 150 mL. Samples were quantitated following a 15-min incubation or while absorbance remained in the linear absorbance detection range. Each sample was tested in triplicate. Samples were monitored for absorbance at 405 nm. Absorbance was plotted versus protein concentration.

Nuclear Magnetic Resonance (NMR) Spectroscopy. Samples for NMR measurements had been lyophilized and redissolved in ^1H_2O or ^2H_2O immediately before the experiment. For work in ^1H_2O solutions, 10% ^2H_2O was routinely used. The final PF4 concentration was 18 mg/mL. The pH was adjusted to pH 5.9 by adding microliter increments of NaO^2H or ^2HCl to a 0.6-mL sample. The pH was not adjusted for isotope effects.

NMR spectra were recorded in the Fourier mode on a Bruker AMX-600 spectrometer (600 MHz for protons). The ^2H_2O deuterium signal was used as a field-frequency lock. All chemical shifts are quoted in parts per million (ppm) downfield from sodium 4,4-dimethyl-4-silapentane sulfonate (DSS).

For sequential assignments, COSY (Aue et al., 1976; Wider et al., 1984), double quantum filtered COSY (Piantini et al., 1982; Shaka & Freeman, 1983), and NOESY (Jeener et al., 1979; Wider et al., 1984) experiments (mixing times of 0.05, 0.075, 0.1, and 0.2 s) were performed. 2D-Homonuclear magnetization transfer (HOHAHA) spectra, used to identify many spin systems completely, were obtained by spin-locking with a MLEV-17 sequence (Bax & Davis, 1985) with mixing times of 30−60 ms. All spectra were acquired in the phase-sensitive mode by using TPPI or States-TPPI (Wüthrich, 1986; States et al., 1982). The water resonance was suppressed by direct irradiation (0.6 s) at the water frequency during the relaxation delay between scans

as well as during the mixing time in NOESY experiments, or by using a square-shaped pulse (100 ms for 0.6 s) defined by 1024 points.

The majority of 2D-NMR spectra were collected as 512 or 1024 t_1 experiments, each with 1K or 2K complex data points over a spectral width of 6 kHz in both dimensions with the carrier placed on the water resonance. Sixty-four or 96 scans were generally time averaged per t_1 experiment. The data were processed directly on the Bruker AMX-600 X-32 or offline on a Bruker Aspect-1 workstation with the Bruker UXNMR data processing program. Data sets were multiplied in both dimensions by 0−60° shifted sine-bell or Lorentzian to Gaussian transformation functions and generally zero-filled to 1K in the t_1 dimension prior to Fourier transformation.

2D- and 3D-NMR and $^1H-^{15}N$ TOCSY-HMQC experiments (Marion *et al.*, 1989a,b; Driscoll *et al.*, 1990; Fesik & Zuiderweg, 1990) were acquired using direct irradiation or square-shaped pulses (100 ms for 0.6 s) of 1024 points for suppression of the water signal. NOESY-HMQC experiments were acquired using mixing times of 100 and 200 ms. The ^1H carrier was placed at the water frequency, and the ^{15}N carrier was placed at 125.0 ppm. The acquired data matrices for each 3D experiment were 128 (t_1) × 32 (t_2) × 1024 (t_3) complex data points, with spectral widths of 7200, 3600, and 7200 Hz in the $F_1(^1H)$, $F_2(^{15}N)$, and $F_3(^1H)$ dimensions, respectively. The spectra were recorded in pure absorption mode using the TPPI and TPPI−States methods for quadrature detection in t_1 and t_2, respectively. Zero-filling was employed to yield spectra of 512 (F_1) × 64 (F_2) × 1024 (F_3) points. Additional suppression of the water signal was achieved by convolution of the time-domain data (Marion *et al.*, 1989c).

A high-resolution 2D $^1H-^{15}N$ HSQC experiment (Bodenhausen & Ruben, 1980) was acquired (4096 × 1024) in order to measure the $^3J_{HN-H\alpha}$ coupling constants. For this experiment, protons were not decoupled during the t_2 evolution, thereby allowing $^1H-^1H$ couplings to evolve during acquisition. The ^1H and ^{15}N carriers were placed at the water frequency and 125.0 ppm, respectively, with spectral widths of 3600 (^1H) and 3648 Hz (^{15}N). The O1 for the ^1H dimension was centered within the NH resonance region. The water resonance was folded over in the downfield region of the spectral window. Water was saturated by using phase-shifted square-shaped pulses (100 ms for 0.6 s) of 1024 points. The TPPI−States method was used to obtain quadrature detection in both the t_1 and t_2 dimensions. Zero-filling yielded a final spectrum of 4K × 2K points.

Interproton distance constraints were derived from NOEs assigned in 2D ^1H homonuclear and 2D and 3D $^1H-^{15}N$ heteronuclear edited NOESY spectra acquired with mixing times of 50, 75, 100, and 200 ms. Analysis of NOE growth curves indicated that while backbone to backbone interproton NOEs were normally maximum at 75−100 ms, side chain to side chain and some side chain to backbone NOEs were maximum at 100−200 ms. Generally, NOEs were classified as strong, medium, weak or very weak using 75−100-ms NOESY data sets, corresponding to upper bound distance constraints of 2.8, 3.3, 4.0, and 4.5 Å, respectively. The lower bound restraint between nonbonded protons was set to 1.8 Å. Pseudoatom corrections were added to the upper bound distance constraints where appropriate (Wüthrich et al., 1983), and a 0.5-Å correction was added to the upper bound for NOEs involving methyl protons (Tropp, 1980; Koning et al., 1990). Averaging was applied to NOEs involving non-stereospecifically assigned methylene protons (Brunger et al., 1986; Clore et al., 1986). For $^3J_{HN-H\alpha} > 8$ Hz and < 5 Hz, the ϕ angle was restrained to be $-120 \pm 40°$ and $-65 \pm 25°$, respectively. The minimum range employed for ϕ dihedral angle constraints was ±25°. Stereospecific assignments of β-methylene protons were derived from interproton distances obtained from 2D NOESY and 3D ^{15}N-edited NOESY experiments and from qualitative estimates of the magnitude of some $^3J_{H\alpha-H\beta}$ coupling constants obtained from 2D TOCSY, DQF- COSY, and 3D ^{15}N-edited TOCSY experiments.

Hydrogen bond constraints were identified from the pattern of sequential and interstrand NOEs involving NH and $C_\alpha H$ protons, together with evidence of slow amide proton−solvent exchange. Exchange of amide protons was monitored with a series of HOHAHA experiments performed at 20 °C and pH 4.6. Peptide was first exchanged and freeze-dried from ^1H_2O solution. ^2H_2O at ice bath temperature was then added to the dried peptide kept in the NMR tube on ice. A HOHAHA experiment was run for approximately 3 h, collecting 256 time-incremented 1K data point FIDs, each with 32 transients. Data sets were first multiplied in both dimensions by a 30° shifted sine-squared bell function and zero-filled to 512 in the t_1 dimension prior to Fourier transformation. Long-lived backbone amide protons were identified by comparing cross-peak positions to sequentially assigned HOHAHA data sets accumulated under the same conditions, but in the presence of 90%/10% $^1H_2O/^2H_2O$ where NH resonances were present. αN cross-peaks which remained during the ^2H_2O HOHAHA accumulation are called "long-lived" in this paper—the larger the cross-peak, the longer the relative lifetime. Each hydrogen bond identified was defined using two distance constraints, $r_{NH-O} = 1.7-2.3$ Å and $r_{N-O} = 2.5-3.3$ Å, except for those hydrogen bonds which occur at the ends of secondary structure units, in which $r_{NH-O} = 1.7-2.4$ Å and $r_{N-O} = 2.5-3.4$ Å.

Computer Modeling. NMR/NOE-derived internuclear distance constraints were used in calculating structures for PF4-M2 by using the X-PLOR suite of programs (Brünger, 1992). Monomeric PF4-M2 was created using parallhdg.pro force fields. The monomer was then duplicated into A, B, C, and D subunits for the PF4-M2 tetramer. Since, unlike native tetrameric PF4 (Zhang et al., 1993; see also Results), the PF4-M2 tetramer is symmetric, having three C2 axes, a symmetry table was created and noncrystallographic symmetry (NCS) restraints were applied for residues 8−68, but not for the less structured N-terminal segment residues 1−7. A 0.1-Å variation between monomers was allowed. For NOE constraints, a soft potential function was used.

The first step in our X-PLOR protocol created a template coordinate set by using the Template routine. Then 80 random structures were generated and refined using the Random and Refine routines, respectively. This dynamical simulated annealing procedure ran high-temperature dynamics (2000 K for 50 ps), cooled down (to 100 K in 50 K steps with 1.3 ps of molecular dynamics at each temperature step), and energy minimized the structures. The distance symmetry force constant was kept at 1.0 kcal mol^{-1} $Å^{-2}$ throughout the calculation. The NCS force constant for the first phase of the simulated annealing protocol was kept at 0.1 kcal mol^{-1} $Å^{-2}$. The NOE force constant was increased by a

Table 1: Structural Statistics

RMS deviationsfrom experimental distance restraints (Å)[a]	
NOE (858/monomer)	0.07 + 0.005
H-bond (32/monomer)	
deviations from idealized geometry	
bonds (Å)	0.004
angles (deg)	0.77 ± 0.03
impropers (deg)	0.62 ± 0.04
energies (kcal mol^{-1})	
E_{NOE}[b]	67 ± 5
E_{CDIH}	9 ± 2
E_{NCS}	8 ± 1.3
E_{bond}	19 ± 1.8
E_{angle}	198 ± 15
$E_{improper}$	33 ± 4
E_{total}	413 ± 42

[a] None of the 27 final structures exhibited distance restraint violations greater than 0.3 Å or dihedral angle violations greater than 10°. RMSD values represent the mean and standard deviations for the 27 structures. [b] The final values of the NOE (E_{NOE}), torsion angle, (E_{CDIH}) and NCS (E_{NCS}) potentials have been calculated with force constants of 25 kcal mol^{-1} Å^{-2}, 200 kcal mol^{-1} rad^{-2}, and 300 kcal mol^{-1} Å^{-2}, respectively.

factor of 2 at the beginning of each cycle, from an initial value of 2 to a maximum value of 25 kcal mol^{-1} Å^{-2}, while the van der Waals force constant was increased slowly from 0.01 to 4 kcal mol^{-1} Å^{-2}. Powell minimization was then performed at 100 K for 250 steps. The resulting structures were subjected to the same Refine routine three times. Significant reductions in E_{total} and E_{NOE} were noted with each Refine cycle.

These structures then were superimposed using the BIOSYM INSIGHT viewer and analyzed using X-PLOR analysis routines. Thirty-four structures with the lowest rmsd values were selected for final X-PLOR refinement where the temperature gradient ran from 1000 to 100 K with 1.3 ps of dynamics at every 50 K step. Powell minimization was performed for 1000 steps. Final structures were subjected to the X-PLOR Accept routine with the violation threshold for NOEs and dihedral angles as shown in Table 1. Twenty-seven structures showed fewer than five violations for an NOE threshold of 0.3 Å and no dihedral angle violations with a threshold of 10° (Nilges, 1993). All computations were performed on Silicon Graphics (SGI) 4 R-4400 Challenge L CPUs and analyzed on SGI Indigo Extreme workstations.

Aggregate-State Populations from Line-Fitting Analyses. For native PF4 and PF4-M2, Y60 ϵH_2 resonances in M−D−T states are relatively well resolved and are used here to obtain aggregate state populations and equilibrium association binding constants for dimer and tetramer formation as discussed by Mayo and Chen (1989) and Mayo (1991). Resonance area integrals were derived by Gaussian/Lorentzian line fitting of NMR spectra on the Bruker AMX-600 spectrometer X-32 computer using standard Gaussian/Lorentzian functions. A baseline was established by comparing fits with the noise level where no resonances were found on both sides of the aromatic resonance region. Baselines were generally flat. Errors in fitting monomer−dimer−tetramer (M−D−T) resonances were less than 10%. These errors have been estimated by allowing individual line fit areas to vary and by observing the effect on spectral traces (Lorentzian/Gaussian summation). To increase the level of confidence in T/D (and D/M) ratios, two protein concentrations were normally analyzed in a similar way.

RESULTS AND DISCUSSION

Native PF4. Figure 2 compares 2D $^1H-^{15}N$ HSQC NMR contour plots of uniformly ^{15}N-enriched tetrameric native PF4 and PF4-M2. For native PF4 (Figure 2), multiple and/or asymmetric cross-peaks are observed, in contrast to the $^1H-^{15}N$ HSQC spectrum of PF4-M2 (Figure 2). In the region where gylcine $^1H-^{15}N$ correlations normally are found, for example, some eight or nine cross-peaks can be observed. Native PF4 has only three glycines, G5, G33, and G48. While some of this cross-peak multiplicity could be the result of *cis/trans* proline isomerization, PF4-M2 shows none of these spectral characteristics, and dissociation of tetrameric native PF4 to the monomer state (Mayo & Chen, 1989) removes this multiplicity (data not shown). Mixed M−D−T aggregate states (Mayo & Chen, 1989) is another possible explanation for this multiplicity/broadening; however, at these PF4 and PF4-M2 concentrations, tetramers predominate [see Mayo and Chen (1989) for native PF4; see below for PF4-M2]. Therefore, it may be concluded that native PF4 forms asymmetric tetramers in solution as it does in the crystal state (Zhang et al., 1994).

One question is whether or not the structural asymmetry in native PF4 in the crystal is the same in solution. In the human PF4 crystal state, AB-type dimers superimpose well, whereas AC- and AD-type dimers do not. Figure 1 exemplifies this by showing AC and AD dimer sets (Zhang et al., 1994) (Figure 1). One subunit from each dimer has been superimposed on the other. The AC and AD dimer contact sequences are the N-terminus residues and turn/loop residues R22−S26, G33−T38, and T44-R49 (Zhang et al., 1994). All three glycines in native PF4 (G5, G33, G48) are found in these contact regions. For native PF4 in solution, some 8−9 glycine $^1H-^{15}N$ cross-peaks can be observed (Figure 2A). Another residue in one these contact regions is T25, which shows about 4 such cross-peaks (Figure 2A) compared to the same spectral region for PF4-M2. For the β-sheet domain where residue contacts are less, multiplicity appears to be less, although cross-peaks are broadened and/or asymmetric, as exemplified with A43 and other β-sheet residues when compared to data on PF4-M2 in Figure 2B. At least for these most easily analogously assignable cross-peaks, it appears that similar regions are affected in both crystal and solution states. This supports the idea of similar (if not identical) crystal and solution quarternary structures for native PF4.

NMR structural elucidation of native PF4 was deemed impossible since it would involve sequence-specific resonance assigments and conformational analysis of 70 residues, each potentially showing 4 individual cross-peaks. This could be equivalent to analysis of a 280-residue protein.

Since the highly negatively charged N-terminal sequences, i.e., E^1AEEDGDLQC^{10} LC..., in AC (BD) dimers are proximal (Zhang et al., 1994), and since electrostatic interactions do contribute to protein folding differences in native human PF4 (Barker & Mayo, 1995), we hypothesized that electrostatic interactions with these sequences could contribute to, if not explain, the observed native PF4 tetramer asymmetry. To test this hypothesis, we examined a chimeric mutant of PF4, called PF4-M2, which has the native PF4

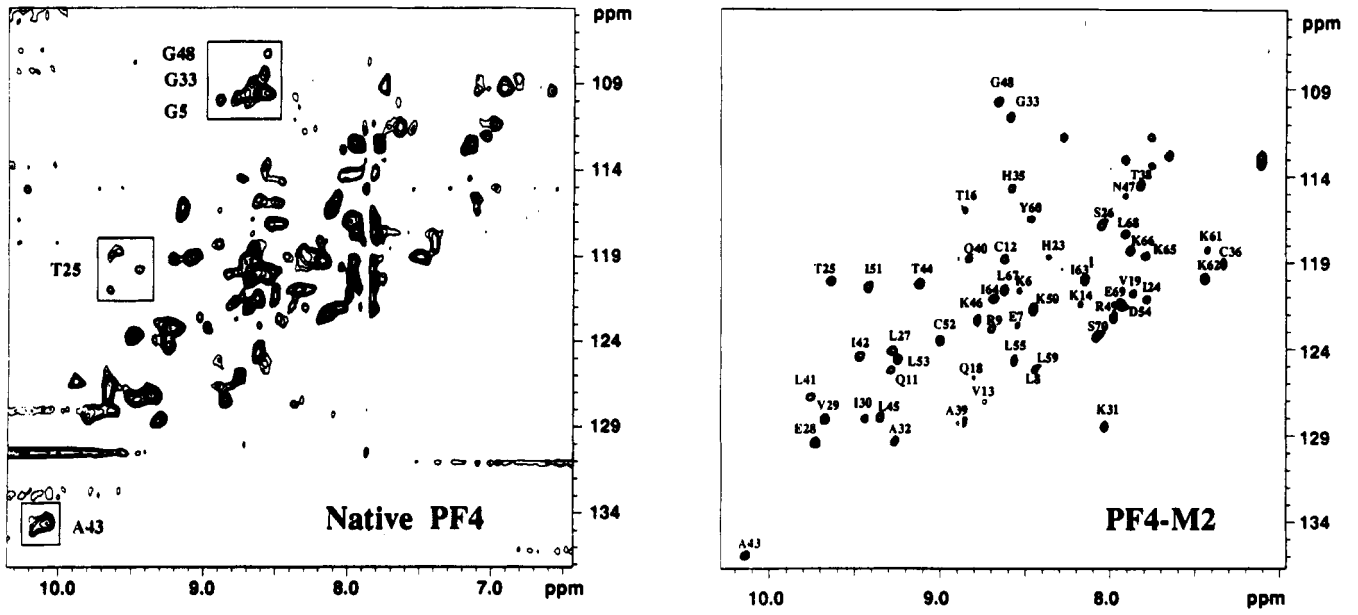

FIGURE 2: 2D $^1H-^{15}N$ HSQC spectra of native PF4 (A) and PF4-M2 (B) at 50 °C enriched in ^{15}N. Data were collected by placing the ^1H carrier in the center of the NH region and the ^{15}N carrier at 125 ppm. The sweep width in the proton dimension is 3600 Hz and in the nitrogen dimension is 3600 Hz. The water is folded in the sparse region of the NH protons. The water is suppressed by using a 100-ms phase-shifted square-shaped pulse defined by 1024 points for 600 ms.

sequence from the CXC residues to the C-terminal serine, but substitutes the IL-8 N-terminal sequence SAKELRCQC... for the native PF4 N-terminal sequence. For consistency and ease of discussion, PF4-M2 residues are numbered from 3 to 70. The net charge up to C10 has been changed from −4 (native PF4) to +2 (PF4−M2). $^1H-^{15}N$ HSQC cross-peaks for PF4-M2 are very well defined, symmetric, and not broadened. In fact, the expected number of cross-peaks for PF4-M2 is observed. This indicates that PF4-M2 is either monomeric or forms symmetric dimers or tetramers in solution. The sequence-specific resonance assignments shown are discussed below.

PF4-M2 Subunit Association Equilibria. To assess the aggregation state(s) of PF4-M2, several approaches were used. Gel filtration profiles (data not shown) suggest aggregate formation at the concentrations used above. Assuming ideal column behavior, the position of the main peak suggests the presence of mostly tetramers. This is consistent with the known aggregation properties of native PF4 (Mayo & Chen, 1989). However, when PF4-M2 was chemically cross-linked with DSS and analyzed by SDS gel electrophoresis (data not shown) under reducing conditions, the major aggregate species was dimer, with minor contributions from tetramer species. This was somewhat surprising, but may be explained by considering that cross-linking can produce more intermediate aggregate species as opposed to the final aggregate state. Furthermore, this technique only gives a qualitative distribution of aggregate states and does not necessarily represent a true equilibrium distribution.

Like native PF4 (Mayo & Chen, 1989), LA-PF4 (Mayo, 1991), and NAP-2 (Yang et al., 1994), PF4-M2 (at lower concentrations and lower pH values than noted above) gives proton NMR spectra (600 MHz) which show the presence of slow exchange (NMR chemical shift time scale) among monomer−dimer−tetramer aggregate states (data not shown). Assignments to M−D−T states could be made on the basis of tyrosine (Y60) ϵH_2 resonance intensity changes as a function of protein concentration using the procedure of Mayo and Chen (1989) and Mayo (1991).

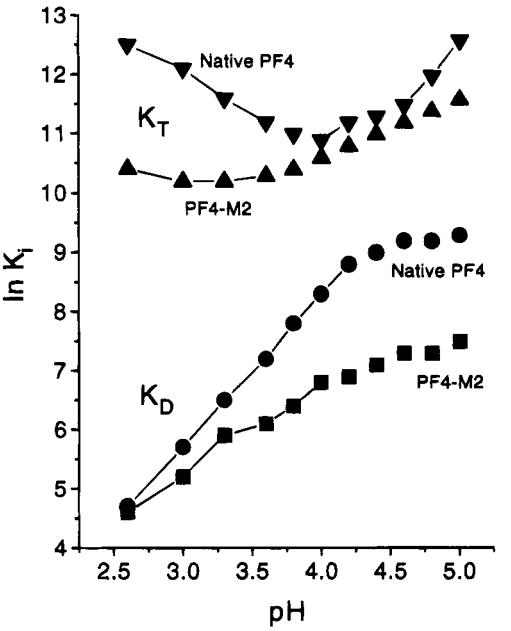

FIGURE 3: Equilibrium subunit association constants for PF4-M2 and native PF4. Equilibrium constants were derived as discussed in the text and in Mayo and Chen (1989) and Mayo (1991).

To compare subunit association properties of native PF4 and PF4-M2, apparent equilibrium constants for dimer and tetramer association were derived as discussed by Mayo and Chen (1989) and Mayo (1991) from steady-state M, D, and T resonance populations by considering the general equilibrium expressions

$$K_D = [D]/[M]^2 \quad \text{and} \quad K_T = [T]/[D]^2 \qquad (1)$$

M−D−T populations were taken from line fit analyses of Y60 ϵH_2 resonances as discussed in Materials and Methods.

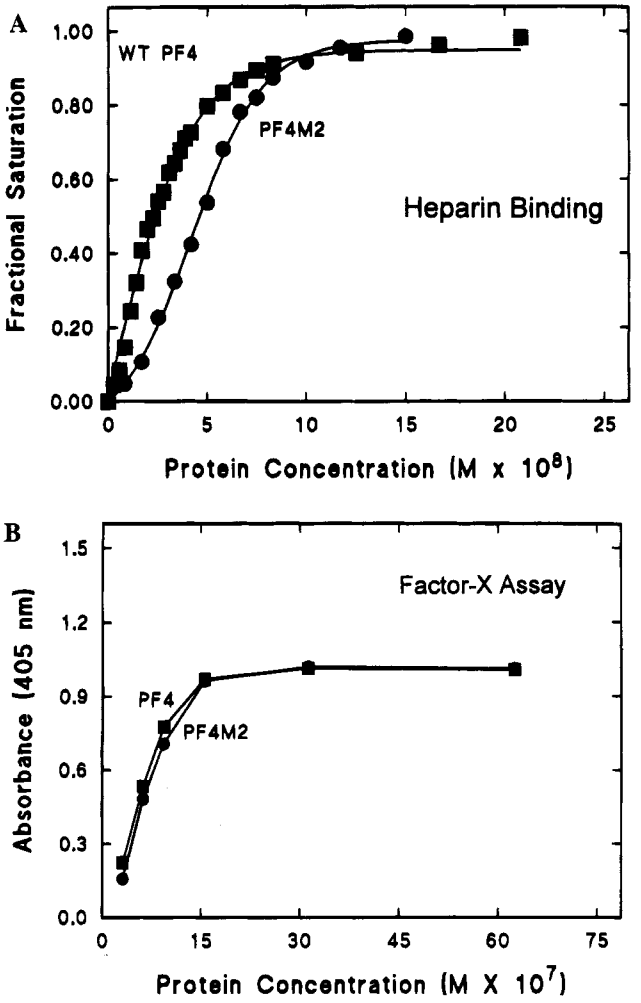

FIGURE 4: Native PF4 and PF4-M2 bioactivity data. Heparin binding (A) and factor X activity (B) data for native PF4 and for PF4-M2 are shown. Data were acquired as discussed in Materials and Methods.

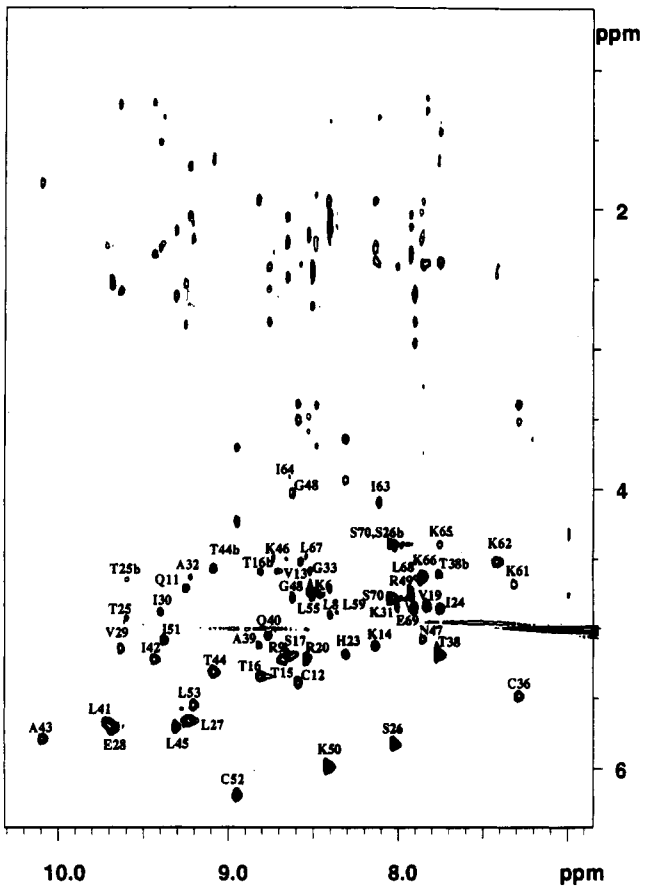

FIGURE 5: HOHAHA of PF4-M2. A 2D-NMR HOHAHA contour plot is shown for PF4-M2, pH 5.9, at 50 °C and 20 mM NaCl in 90% H_2O/10%D_2O. The spin-lock mixing time was 40 ms. Acquisition data size was 2048 × 512, and processed data size was 2048 × 1024. Water suppression was achieved by using a 100-ms square-shaped pulse of 1024 points for 600 ms. Data were processed using a shifted sine-bell function in both dimensions. Resonances and cross-peaks are labeled as described in the text.

The natural logarithms of K_D and K_T are plotted in Figure 3 as a function of solution pH. Data points are average values from two or three separate runs. As the pH is increased, K_D values increase and plateau off above about pH 4. For dimer associations at pH 5, the observed K_D difference translates into a 1.4 kcal mol^{-1} difference in the free energy of association. Since at lower pH K_D values for the two species converge, it may be concluded that electrostatic interactions modulate dimer stability most likely via salt bridge formation in native PF4. K_T values for native PF4 and PF4-M2 behave similarly above about pH 4 by increasing with increasing pH. Below pH 4, however, K_T for native PF4 increases with decreasing pH, while K_T for PF4-M2 remains mostly flat. Thermodynamically, these equilibrium constants indicate that asymmetrically associated native PF4 subunits with the highly negatively charged N-terminus form more stable tetramers than do PF4-M2 subunits. Since PF4-M2 does not show any significant increase in K_T on lowering the pH, the increase in native PF4 dimer−dimer affinity at lower pH is the result of N-terminal carboxylate protonation as previously proposed (Mayo & Chen, 1989).

PF4-M2 Heparin Binding and Other Bioactivities. For native PF4 and PF4-M2, the fraction of protein-bound heparin versus the protein concentration is shown in Figure 4A. The apparent equilibrium dissociation constants for native PF4 and PF4-M2 heparin binding, i.e., K_{HEP}, are 2×10^{-8} and 5×10^{-8} M, respectively. These values represent the PF4 concentration (in moles of monomer) at half-fractional saturation. Although K_{HEP} for PF4-M2 is about a factor of 2 less than that for native PF4, PF4-M2 performed as well as native PF4 in the factor X heparin binding assay (Figure 4B). These heparin binding data indicate that PF4-M2 is essentially functionally the same as native PF4.

Endothelial cell proliferation and elastase release assays (Lewis et al., 1993) (data not shown) indicate that PF4-M2, which contains the IL-8 N-terminal ELR tripeptide, is nearly as active as IL-8 in promoting endothelial cell proliferation and elastase release. Clark-Lewis et al. (1993) showed that similar PF4 N-terminal chimera that contain the ELR sequence are also active in these assays. Their N-terminal chimera had the sequences ELRCLC... and EAEEDGELR-CLC.... PF4-M2 differs in this respect in that it contains the complete IL-8 N-terminal peptide SAKELRCQC....

Sequence-Specific NMR Assignments for PF4-M2. Sequence-specific proton resonance assignments for PF4-M2 were performed initially by using established procedures (Wüthrich, 1986). Spin systems were identified by analyzing HOHAHA and DQF-COSY spectra and sequentially assigned using NOESY spectra. Ambiguities arising from chemical shift degeneracies were resolved by recording spectra at different temperatures from 30 to 50 °C. A typical

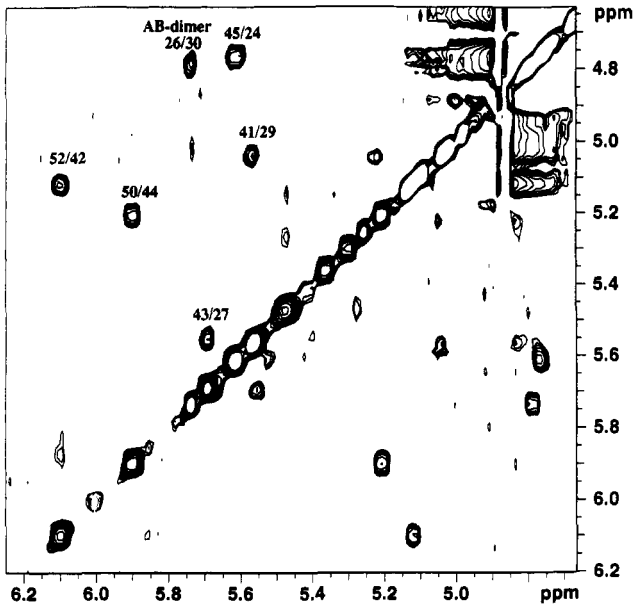

FIGURE 6: NOESY of PF4-M2 αH−αH resonance region. The αH−αH resonance region from a NOESY contour plot is shown for PF4-M2, pH 5.9, at 50 °C. Data were collected in 90% ^1H_2O/10% ^2H_2O. Protein concentration was 18 mg/mL. 512 hypercomplex FIDs containing 1K words were collected and processed as discussed in Materials and Methods. The mixing time was 100 ms. The data were zero-filled to 1024 in t_1. The raw data were then multiplied by a 30° shifted sine-squared function in t_1 and t_2 prior to Fourier transformation. Labeling of resonances is as discussed in the text.

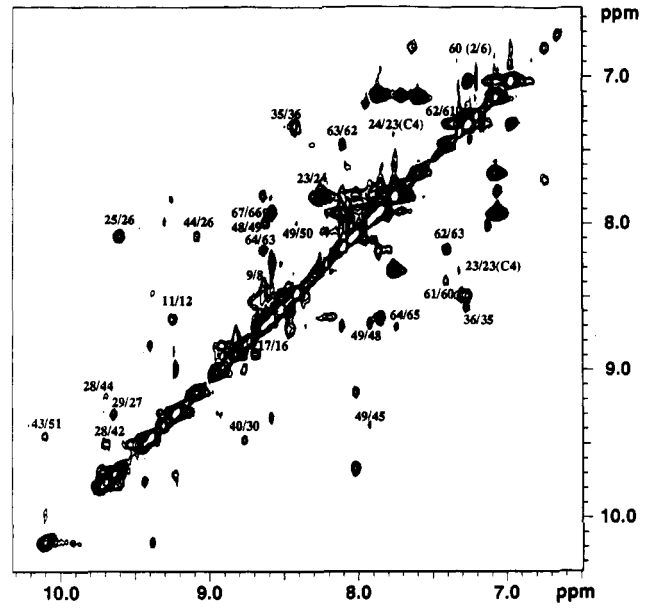

FIGURE 7: NOESY of PF4-M2 NH−NH resonance region. The NH−NH resonance region from a NOESY contour plot is shown for PF4-M2, pH 5.9, at 50 °C. Data were collected and processed as described in the caption of Figure 5. Labeling of resonances is as discussed in the text.

HOHAHA contour plot is shown in Figure 5 with most sequential assignments labeled. Due to the presence of crowded regions and overlap of some αH resonances with the HDO resonance, not all αN cross-peaks have been labeled. To complete remaining assignments and to confirm others, 2D and 3D $^1H-^{15}N$ heteronuclear NMR experiments were performed. These included 2D $^1H-^{15}N$ HSQC experiments as shown in Figure 1, as well as 2D $^1H-^{15}N$ HMQC NOESY and TOCSY and ^{15}N-edited 3D NOESY and TOCSY experiments. Sequence-specific ^1H and ^{15}N resonance assignments are available as supporting information.

PF4-M2 Structure. NOESY spectra are exemplified in Figures 6 and 7, which show the αH−αH and NH−NH regions, respectively. αH−αH connectivities indicate the presence of anti-parallel β-sheet structure, and a continuous series of NH−NH connectivities within the C-terminal domain is consistent with the presence of helix conformation. Further elements of secondary structure can be deduced from a qualitative interpretation of NOE $^3J_{\alpha N}$ coupling constants and long-lived backbone NHs presented in Figure 8. Long-range NOEs between residues are summarized in Figure 9. These NOEs indicate folding of the three-stranded β-sheet: residues 26−31 (strand 1); residues 39−45 (strand 2), and residues 50−53 (strand 3). Y60, E69, and S70 provide some of the best constraints to fix the C-terminal helix (residues 59−70) on top of the β-sheet scaffold.

A total of 858 nonredundant, intramonomer subunit NOE distance constraints were derived from analysis of NOESY spectra as described in Materials and Methods. These include 420 intraresidue, 148 sequential, 123 medium-range ($|i-j| < 5$), and 167 long-range ($|i-j| \geq 5$), constraints. In addition, torsion angle constraints were obtained for 42 φ angles. A total of 16 hydrogen bonds could be identified by inspection of initial PF4-M2 structures, giving rise to 32 hydrogen bond distance constraints. These hydrogen bond constraints account for the slowly exchanging amide protons identified. The total number of experimentally derived constraints was therefore 932, giving a total of 13.3 constraints per residue. Intersubunit distance constraints were initially identified from knowledge of existing CXC chemokine structures as outlined in the introduction. For AB-type dimer contacts, 44 constraints were used in DG calculations, while for AC- and AD-type dimer contacts, only 16 and 8 constraints, respectively, could be found. Addition of these constraints increased the average number of constraints per residue to 14.4.

Structural statistics for the final 27 dynamical simulated annealing structures of PF4-M2 are summarized in Table 1, and best fit superpositions of the backbone C_α atoms are shown in Figure 10 for the tetramer with one AB-type dimer lying on top of the other (Figure 10, left) and then rotated by 90° (Figure 10, right). The less structurally defined N-terminus is clearly apparent, as are the four C-terminal helices running antiparallel to each other at the top and bottom in Figure 10 (right). The six- stranded antiparallel β-sheet domain of one AB-type dimer crosses the other at an angle of about 36° (Figure 10, left). Figure 11 shows views for AB-, AC-, and AD-type dimers and indicates some contact residues in each pair. The structures satisfy experimental constraints very well. No bad nonbonded contacts were found. Backbone and side-chain rmsd values are plotted versus the residue number in Figure 12. Excluding N-terminal residues 3−9 which are least well defined by the data, atomic rms differences for the 27 structures with respect to the mean coordinate positions are 0.54 Å for the backbone (N,C^α, and C) atoms and 1.35 Å for all heavy atoms. For the three β-sheet strands (T25−A32, T38−T44, and K50−L53) as well as for the loop connecting strands 2 and 3 (residues L45−R49), the average backbone rmsd value is 0.42 Å. In addition, φ and ψ angular order parameters are all >0.8 (data not shown). The angular order parameter is

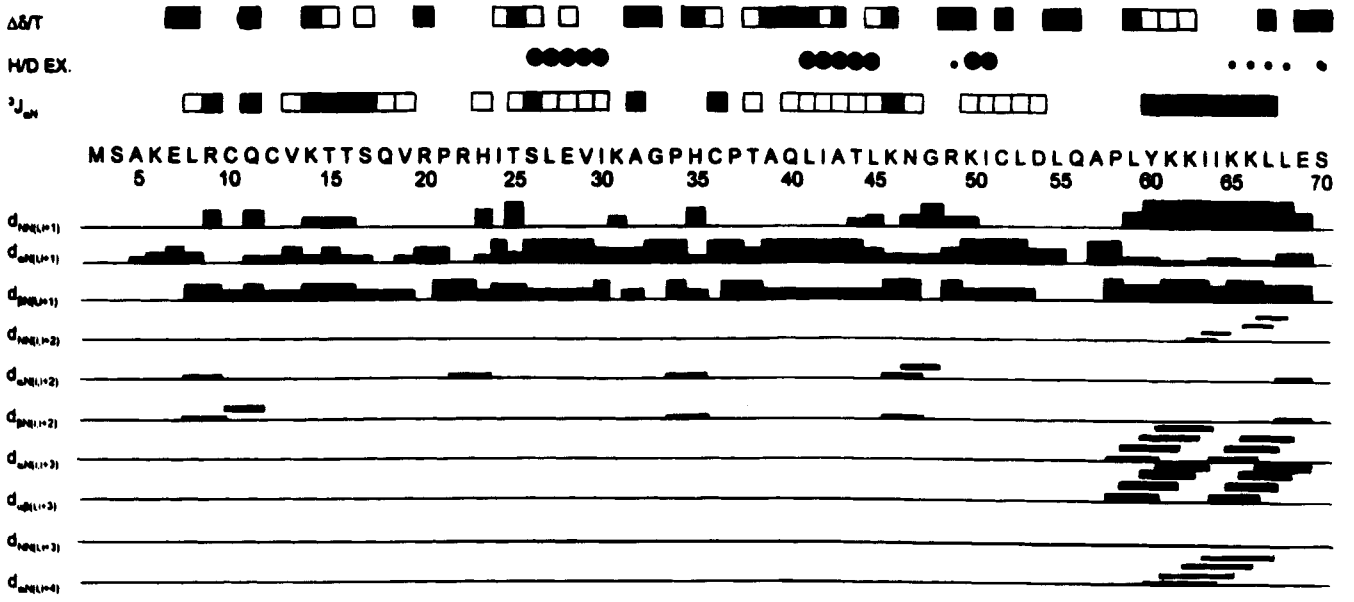

FIGURE 8: Summary of NMR/NOE data for PF4-M2. The PF4-M2 protein sequence is shown with a summary of key NOEs for data accumulated at pH 5.9 and 50 °C. NOEs are tabulated in the format discussed by Wüthrich (1986). $^3J\alpha_N$ coupling constants are indicated with an open square for those greater than 8 Hz and with a closed square for those less than 5.5 Hz. Other coupling constants could not be discerned or fell within the 5.5−8-Hz range. Long-lived backbone NHs are indicated with closed circles; the larger the circle, the longer the lifetime. Temperature factors are shown with an open square for those greater than 8 ppb/K and with a closed square for those less than 5 ppb/K.

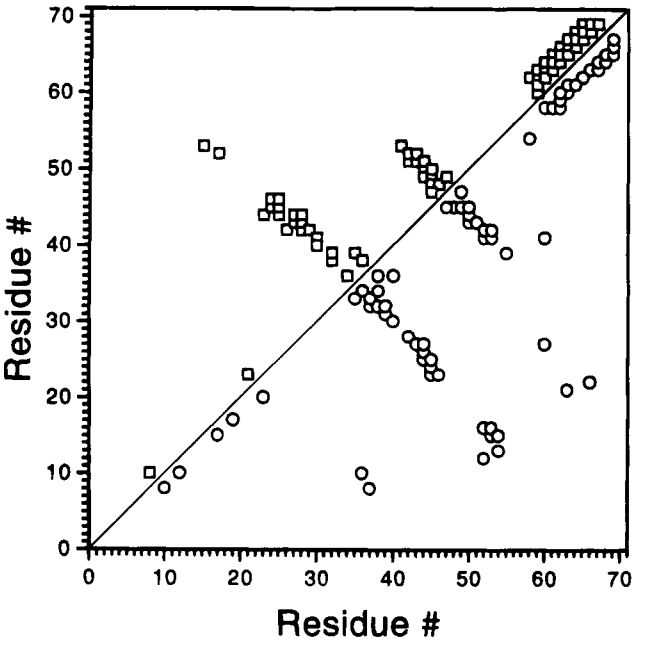

FIGURE 9: Longer range NOEs: Diagonal plot of NOEs for any two nonsequential residues. The residue number is plotted on both axes. Above the diagonal are shown NOEs between backbone αH and NH resonances. Below the diagonal are shown NOEs between backbone/side-chain and side-chain resonances. Each square connects pairs of residues linked by one or more NOE constraints.

defined such that a value of 1 indicates an exactly defined angle while a value of 0 results from complete dihedral heterogeneity (Hyberts et al., 1992). The backbone torsion angles for all non-glycine residues from 9 to 70 lie within the allowed region of a Ramachandran ϕ, ψ plot. Together, the above data indicate that the 27 structures used to represent the solution structure of PF4-M2 are well converged.

Each PF4 monomer subunit contains a triple-stranded antiparallel β-sheet arranged in a "Greek key" with strand 2 (residues 39−45) hydrogen bonded to strands 1 (residues 26−31/32) and 3 (residues 50−53). Strands 1 and 2 are connected by a loop (residues 33/34−38) which shows elements of a turn centered at residues 35−36. Strands 2 and 3 are connected by a 3:5-hairpin (residues 46−49) comprising a β-turn and G1 β-bulge (Sibanda & Thornton, 1985). As evidenced by strong $\alpha H_{(i,i-1)}-\delta H_i$ NOEs, all four proline residues, P21, P34, P37, and P58, have their peptide bonds in the *trans* conformation. Apparent turns are also centered around residues 10−11, 13−14, 17−18, and 55−56. A helix-like conformation within residues 22−25 leads into β-sheet strand 1. The α-helix in PF4-M2 extends from residue 58 to residue 70 within each subunit. C-Terminal residue S70 is well defined by the data and not disordered in solution, indicating that it is motionally restricted.

The antiparallel β-sheet domain and the turn between strands 2 and 3 are either mostly buried or masked by folding of the C-terminal helix and the N-terminus segment (about 20 residues). In addition, the longest lived NHs are found within the sheet region. This β-sheet domain contains the PF4 folding initiation site (Ilyina et al., 1994) and can fold independently of the remainder of the sequence (Ilyina & Mayo, 1995). This suggests that the β-sheet domain forms the protein folding core and functions as a scaffold onto which "functional" residues in the C-terminal heparin binding and N-terminal neutrophil activating (IL-8 receptor binding) domains are folded. The first and third β-sheet turns are generally solvent exposed. Although the N-terminus containing the ELR tripeptide, which is associated with neutrophil activation, is ill-defined probably due to its flexibility, it is folded proximal to the first turn, residues 33−38.

Strand 1 from one subunit interacts in an antiparallel fashion with strand 1′ from the other subunit to form the six-stranded β-sheet AB dimers, which includes the two antiparallel running C-terminal α-helices. The AB dimers are positioned on top of one another at an angle of 36° relative to an average β-sheet axis (Figure 10, left).

FIGURE 10: Superposition of X-PLOR calculated structures. Twenty-seven structures calculated using X-PLOR dynamical simulated annealing protocols as discussed in Materials and Methods and Results are overlayed for tetramer PF4-M2 showing one AB dimer on top and one on the bottom (left overlay) and the same structures rotated by 90° (right overlay).

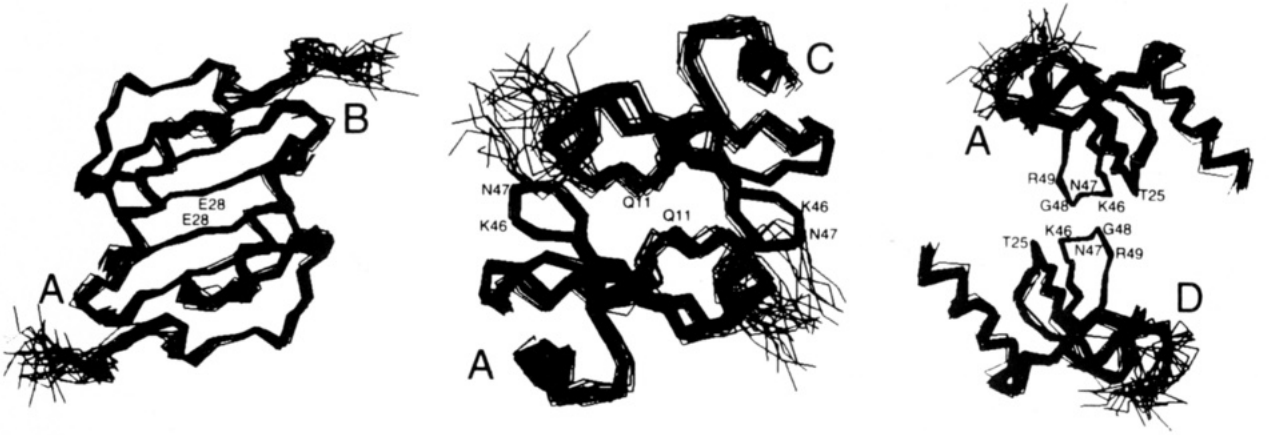

FIGURE 11: Superposition of X-PLOR calculated structures. Twenty-seven structures calculated using X-PLOR dynamical simulated annealing protocols as discussed in Material and Methods and Results are overlayed for PF4-M2 AB-type (left), AC-type (middle), and AD-type dimers (right).

The overall tertiary structural fold (monomer subunit) of PF4-M2 is nearly the same as that reported for the NMR and/or X-ray structures of IL-8 (Clore et al., 1989, 1990; Baldwin et al., 1991), Gro-α (Fairbrother et al., 1994), bovine PF4 (St. Charles et al., 1989), human PF4 (Zhang et al., 1994), and NAP-2 (Mayo et al., 1994). In fact, PF4-M2 quarternary structure in terms of the AB-type dimer is relatively well conserved among all these homologs. Backbone atomic rms deviations were calculated from a best fit superposition between β-sheet residues of PF4-M2 AB-type dimers and those of IL-8 (Clore et al., 1990; Baldwin et al., 1991) and human PF4 (Zhang et al., 1994). Comparison of PF4-M2 and native human PF4 showed that AB-type dimer β-sheet backbone rmsd values ranged from 0.35 to 1.1 Å. For loop residues 32−38 and 54−58, rmsd values increased to 1.2−1.5 and 1.7−2.8 Å, respectively. C-Terminal residues 59−70 were very well defined within themselves, but in this comparison showed 0.8−1.6-Å deviations for residues 59−67 and 2.8−3.5-Å deviations for residue 68−70. These later deviations reflect quarternary structural differences between native PF4 and PF4-M2 and the fact that structural superpositions were optimized for β-sheet residues. For the same reasons, N-terminal residues showed deviations which ranged from 1.8 to 4.2 Å.

Although the distances of closest approach of the helix axes are essentially the same for PF4-M2 and native PF4, i.e., 14 Å, the C-terminus shifts slightly relative to the β-sheet domain. In PF4-M2, this increases the distance between the C-terminal helix residues E69 and S70 of one AB subunit with respect to the other subunit. This increased distance would be expected to significantly weaken or even abolish potential electrostatic interactions between the C-terminal carboxylates and K31, for example, on the opposing subunit and may help to explain the large decrease in dimer equilibrium constants observed for PF4-M2 relative to native PF4 (Figure 3). Unlike tetrameric bovine and human PF4 whose AC and AD subunits associate asymmetrically, PF4-M2 AB dimers associate symmetrically (Figures 1 and 11). Rigid body rotation of one AB-type dimer against the other accounts for most of the displacement and asymmetry in bovine and human PF4. Electrostatic interactions (repulsive and/or attractive) between N-terminal segments and/or other parts of native PF4, therefore, account for the quarternary structural asymmetry.

For PF4-M2 and IL-8 comparisons at the AB dimer level, similar small deviations were noted within the β-sheet domain, whereas rmsd values were larger for the C-terminal helix. Much of the increase in rmsd values arises from

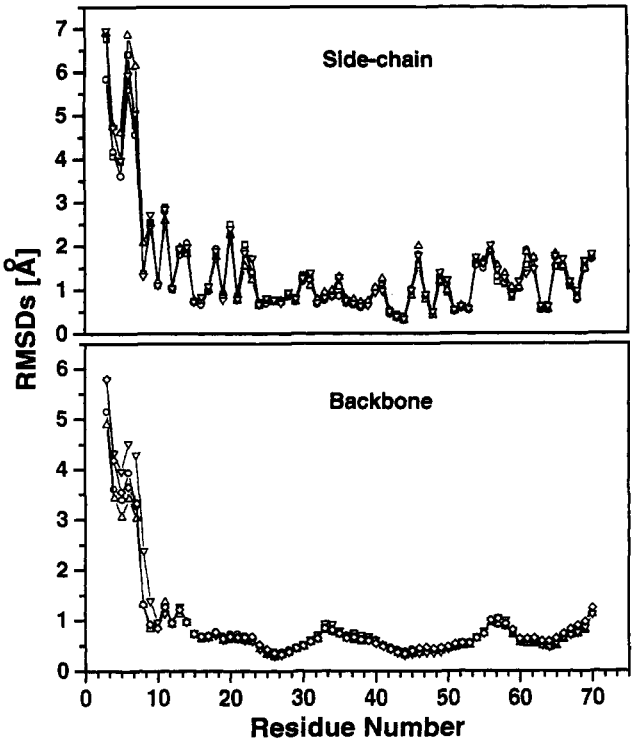

FIGURE 12: RMSD values for PF4-M2. Backbone (bottom) and side-chain (top) rmsd values are plotted versus the residue number in PF4-M2. RMSD values are plotted for each subunit from 27 structures of the tetramer.

differences in positioning of the helix on top of the β-sheet. In IL-8, the distance of closest approach for the AB dimer helices varies from 12.2 Å in the X-ray structure (Baldwin et al., 1991) to 15.3 Å in the NMR structure (Clore et al., 1989; Clore & Gronenborn, 1991). In general, rmsd values at the monomer level are smaller than those made at the AB dimer level.

In terms of heparin binding, this study indicates that native PF4 and PF4-M2 both bind the polysulfated glycosaminoglycan with similar affinity. Structural comparisons show that both the proposed C-terminal helix conformations and the ring of positive charges noted about the tetrameric structure of bovine (St. Charles et al., 1989) and human (Zhang et al., 1994) PF4 are preserved in human PF4-M2. In this respect, it appears that quarternary structural differences between these two PF4 homologs may not be important to the overall heparin binding process. On the other hand, it may be equally possible that heparin interactions are different between native PF4 and PF4-M2, such that somewhat different modes of interaction may coincidentally account for nearly equivalent binding affinities, or it may be that interaction with heparin modifies the PF4 conformation at the tertiary or quarternary structural level. This must await analysis of the PF4-M2 heparin-bound state which is currently underway.

SUPPORTING INFORMATION AVAILABLE

One table giving ^{1}H and ^{15}N chemical shifts for the protein PF4-M2 (3 pages). Ordering information is given on any current masthead page.

REFERENCES

Aue, W. P., Bartholdi, E., & Ernst, R. R. (1976) *J. Chem. Phys. 64*, 2229–2246.

Baldwin, E. T., Weber, I. T., St. Charles, R., Xuan, J.-C., Appella, E., Yamada, M., Matsushima, K., Edwards, B. F. P., Clore, G. M., Gronenborn, A. M., & Wlodawer, A. (1991) *Proc. Natl. Acad. Sci. U.S.A. 88*, 502–506.

Barber, A. J., Kaser-Blanzmann, R., Jakabova, M., & Luscher, E. F. (1972) *Biochim. Biophys. Acta 286*, 312–328.

Barker, S., & Mayo, K. H. (1995) *FEBS Lett. 357*, 301–304.

Bax, A., & Davis, D. G. (1985) *J. Magn. Reson. 65*, 355–360.

Bidlingmeyer, B. A., Cohen, S. A., & Tarvin, T. L. (1984) *J. Chromatogr. 336*, 93–100.

Bock, P. E., Luscombe, M., Marshall, S. E., Pepper, D. S., & Holbrook, J. J. (1980) *Biochem. J. 191*, 769–776.

Bodenhausen, G., & Ruben, D. J. (1980) *Chem. Phys. Lett. 69*, 185–189.

Brunger, A. T. (1992). X-plor (Version 3.1) Manual, Yale University Press, New Haven, CT.

Brunger, A. T., Clore, G. M., Gronenborn, A. M., & Karplus, M. (1986) *Proc. Natl. Acad. Sci. U.S.A. 83*, 3801–3805.

Clark-Lewis, I., Dewald, B., Geiser, T., Moser, B., & Baggiolini, M. (1993) *Proc. Natl. Acad. Sci. U.S.A. 90*, 3574–3577.

Clore, G. M., & Gronenborn, A. M. (1991) *J. Mol. Biol. 217*, 611–620.

Clore, G. M., Brunger, A. T., Karplus, M., & Gronenborn, A. M. (1986) *J. Mol. Biol. 191*, 523–551.

Clore, G. M., Appella, E., Yamada, M., Matsushima, K., & Gronenborn, A. M. (1989) *Biochemistry 29*, 1689–1696.

Clore, G. M., Bax, A., Wingfield, P. T., & Gronenborn, A. M. (1990) *Biochemistry 29*, 5671–5676.

Cowan, S., Bakshi, E. N., Machin, K. J., & Issacs, N. W. (1986) *Biochem. J. 234*, 485–488.

Davie, E. W., Fujikawa, K., & Kisiel, W. (1991) *Biochemistry 30*, 10363–10370.

Deuel, T. F., Keim, P. S., Farmer, M., & Heinrikson, R. L. (1977) *Proc. Natl. Acad. Sci. U.S.A. 74*, 2256–2258.

Deuel, T. F., Senior, R. M., Chuang, D., Griffin, G. L., & Heinrikson, R. L.(1981) *Proc. Natl. Acad. Sci. U. S. A. 78*, 4584–4587.

Driscoll, P. C., Clore, G. M., Marion, D., Wingfield, P. T., & Gronenborn, A. M. (1990) *Biochemistry 29*, 3542–3556.

Fairbrother, W. J., Reilly, D., Colby, T. J., Hesselgesser, J., & Horuk, R. (1994) *J. Mol. Biol.* (in press).

Fesik, S. W., & Zuiderweg, E. R. P. (1990) *Q. Rev. Biophys. 23*, 97–131.

Gerwitz, A. M., Calabretta, B., Rucinski, B., Niewiarowski, S., & Xu, W. Y. (1989) *J. Clin. Invest. 83*, 1477–1486.

Grasberger, B. L., Gronenborn, A. M., & Clore, G. M. (1993) *J. Mol. Biol. 230*, 364–372.

Han, Z. C., Sensebe, L., Abgrall, J. F., & Briere, J. (1990) *Blood 75*, 1234–1239.

Holt, J. C., & Niewiarowski, S. (1985) *Semin. Hematol. 22*, 151–163.

Huang, S. S., Huang, J. S., & Deuel, T. (1982) *J. Biol. Chem. 257*, 11546–11550.

Hyberts, S., Goldberg, M. S., Havel, T. F., & Wagner, G. (1992) *Protein Sci. 1*, 736–751.

Ilyina, E., & Mayo, K. H. (1995) *Biochem. J. 306*, 407–419.

Ilyina, E., Milius, R., & Mayo, K. H. (1994) *Biochemistry 33*, 13436–13444.

Jeener, J., Meier, B., Backman, P., & Ernst, R. R. (1979) *J. Chem. Phys. 71*, 4546–4550.

Koning, T. M. G., Boelens, R., & Kaptein, R. (1990) *J. Magn. Reson. 90*, 111–123.

Loscalzo, J., Melnick, B., & Handin, R. I. (1985) *Arch. Biochem. Biophys. 24*, 446–455.

Lowry, O. H., Rosbough, N. J., Fan, A. L., & Randall, R. J. (1951) *J. Biol. Chem. 193*, 265–270.

Maione, T. E., Gray, G. S., Petro, J., Hunt, A. J., Donner, A. L., Bauer, S. I., Carson, H. F., & Sharpe, R. J. (1990) *Science 247*, 77–79.

Marion, D., Driscoll, P. C., Kay, L. E., Wingfield, P. T., Bax, A., Gronenborn, A. M., & Clore, G. M. (1989a) *Biochemistry 28*, 6150–6156.

Marion, D., Kay, L. E., Sparks, S. W., Torchia, D. A., & Bax, A. (1989b). *J. Am. Chem. Soc. 111*, 1515–1517.

Marion, D., Ikura, M., & Bax, A. (1989c) *J. Magn. Reson. 84*, 425–430.

Mayo, K. H. (1991) *Biochemistry 30*, 925−934.
Mayo, K. H., & Chen, M. J. (1989) *Biochemistry 28*, 9469−9478.
Mayo, K. H., Yang, Y., Daly, T. J., Barry, J. K., & La Rosa, G. J. (1994) *Biochem. J. 304*, 371−376.
Moser, B., Schumacher, C., von Tscharner, V., Clark-Lewis, I., & Baggiolini, M. (1991) *J. Biol. Chem. 266*, 10666−10671.
Myers, J. A., Gray, G. G., Peters, D. J., Grimaila, R. J., Hunt, A. J., Maione, T. E., & Muellar, W. T. (1991) *Protein Expression Purif. 2*, 136−143.
Nilges, M. (1993) *Proteins: Struct., Funct., Genet. 17*, 297−309.
Nilges, M., Clore, G. M., & Gronenborn, A. M. (1988) *FEBS Lett. 239*, 317−324.
Piantini, U., Sørensen, O. W., & Ernst, R. R. (1982) *J. Am. Chem. Soc. 104*, 6800−6805.
Rucinski, B., Niewiarowski, S., James, P., Walz, D. A., & Budzynski, A. Z. (1979) *Blood 53*, 47−62.
Sato, Y., Abe, M., & Takaki, R. (1990) *Biochem. Biophys. Res. Commun. 172*, 595−600.
Shaka, A. J., & Freeman, R. (1983) *J. Magn. Reson. 51*, 161−169.
Sharpe, R. J., Byers, H. R., Scott, C. F., Bauer, S. I., & Maione, T. E. (1990) *J. Natl. Cancer Inst. 82*, 848−853.
Sibanda, B. L., & Thornton, J. M. (1985) *Nature 316*, 170−174.
Smith, P. K., Krohn, R. I., Hermanson, G. T., Mallia, A. K., Gartner, F. H., Provenzano, M. D., Fujimoto, E. K., Goeke, N. M., Olson, B. J., & Klenk, D. C. (1985) *Anal. Biochem. 150*, 76−85.
States, D. J., Haberkorn, R. A., & Ruben, D. J. (1982) *J. Magn. Reson. 48*, 286−293.
St. Charles, R., Walz, D. A., & Edwards, B. F. P. (1989) *J. Biol. Chem. 264*, 2092−2099.
Suda, Y., Sobel, M., Sumi, M., & Ottenbride, R. M. (1990) *J. Bioact. Compat. Polym. 5*, 412−419.
Tropp, J. (1980) *J. Chem. Phys. 72*, 6035−6043.
Waddell, W. J. (1956) *J. Lab. Clin. Med. 48*, 311−314.
Wider, G., Macura, S., Anil-Kumar, Ernst, R. R., & Wüthrich, K. (1984) *J. Magn. Reson. 56*, 207−234.
Wolpe, S. D., & Cerami, A. (1989) *FASEB J. 3*, 2565−2573.
Wüthrich, K. (1986) *NMR of Proteins and Nucleic Acids*, Wiley-Interscience, New York.
Wüthrich, K., Billeter, M., & Braun, W. (1983) *J. Mol. Biol. 169*, 949−961.
Yang, Y., Mayo, K. H., Daly, T. J., Barry, J. K., & La Rosa, G. L. (1994) *J. Biol. Chem. 269*, 20110−20118.
Zhang, X., Chen, L., & Bancroft, D. P. (1994) *Biochemistry 33*, 8361−8366.

BI951112J